Arabian Journal for Science and Engineering
https://doi.org/10.1007/s13369-023-07797-7

RESEARCH ARTICLE-MECHANICAL ENGINEERING

The Developed Conservation Element and Solution Element Method in Two-Dimensional Spherical Coordinate and Its Application to the Analysis of Non-Fourier Heat Conduction

Amir Ghasemi Touran Poshti[1] · **Mohammad Ali Ansari**[2] · **Mohammad Bagher Ayani**[1]

Received: 27 July 2022 / Accepted: 16 February 2023

Abstract

In solving the system of hyperbolic equations, highly accurate numerical methods which are easy to apply and have a shorter run time without causing numerical oscillations are more popular. In the present study, the space–time conservation element and solution element (CESE) method has been developed into two-dimensional spherical coordinates using polar elements. Then, the developed CESE method has been applied to investigate the propagation of a non-Fourier thermal waves in biological tissue. To evaluate the performance of the CESE method, the numerical results are compared to the existing semi-analytical results, and it is observed that the results are in good agreement. The experimental test is then conducted to measure the transient temperature behavior of the spherical Intralipid phantom irradiated by a near-infrared pulsed laser. A comparison of experimental and numerical results demonstrates the applicability of the dual phase lag model in the prediction of non-Fourier heat conduction in biological tissue. In addition, the contours of heat flux and temperature during and after laser irradiation are presented, and the propagation of thermal waves in the tissue is examined and discussed. The results indicate that the effects of the two-dimensional thermal wave appear after stopping the laser irradiation. Finally, the study of the effect of tissue type on wave progression in the tumor, muscle, and fat demonstrates that in the fat tissue, having the lowest thermal diffusivity, the thermal progression is less than the tumor and muscle. However, the temperature distribution in the fat tissue is greater than in the other tissues.

Keywords Conservation element and solution element method · Dual phase lag model · Spherical tissue · Intralipid phantom · Non-Fourier heat conduction

List of Symbols

c	Specific heat of tissue
c_b	Specific heat of blood
$\boldsymbol{F}$	Flux vector in radial direction
$\boldsymbol{G}$	Flux vector in angular direction
$\boldsymbol{H}$	Space–time flux vector
k	Thermal conductivity
$\boldsymbol{q}$	Heat flux vector
$\boldsymbol{q}_{\mathbf{r}}$	Heat flux in radial direction
$\boldsymbol{q}_{\boldsymbol{\theta}}$	Heat flux in angular direction
q_L	Laser intensity
Q_m	Metabolic heat generation
Q_r	Dimensionless heat flux in radial direction
Q_θ	Dimensionless heat flux in angular direction
r	Coordinate variable in radial direction
$\boldsymbol{r}$	2-D position vector
R	Diffuse reflectance
$\boldsymbol{S}$	Source vector
t	Time
T	Temperature of tissue
T_b	Blood temperature
$\boldsymbol{U}$	Primary variable vector

Greek symbols

ζ	Dimensionless radius
η	Dimensionless time

✉ Mohammad Bagher Ayani
mbayani@um.ac.ir

1 Department of Mechanical Engineering, Faculty of Engineering, Ferdowsi University of Mashhad, Mashhad, Iran

2 Optical Bio-Imaging Lab, Laser and Plasma Research Institute, Shahid Beheshti University, Daneshju Boulevard, Tehran, Iran

Published online: 29 March 2023

θ	Coordinate variable in angular direction
θ^*	Dimensionless angle
ρ	Density of tissue
ρ_b	Density of blood
τ_q	Phase lag time of heat flux
τ_T	Phase lag time of temperature gradient
Φ	Dimensionless temperature
ω_b	Blood perfusion rate

1 Introduction

In recent years the applications of short-pulse lasers have been expanded in laser medical treatments, such as laser-induced hyperthermia, laser surgery, and laser-based photothermal therapy (PTT). Inaccurate prediction of temperature distribution and lack of control over temperature rise in the tissues results in damage to surrounding healthy tissues during any laser therapy. Hyperthermia is a type of medical treatment in which the body temperature is exposed to temperatures above the normal range to destroy or ablate specific cells. The best region of the wavelength spectrum to treat hyperthermia is the near-infrared range, where tissue absorption properties exceed those of the blood [1]. Based on the rate of temperature increasing in the tissue, hyperthermia treatments are divided into three categories, long-term low-temperature hyperthermia ($T \leq 41°C$), moderate-temperature hyperthermia ($41°C < T < 46°C$), and high-temperature hyperthermia ($T \geq 46°C$) [2]. The higher the temperature in the tissue, the shorter the irradiation time, and in high-temperature hyperthermia treatment, this time is reduced to 4–6 min. Pennes equation is one of the bio-heat transfer models that analyzes thermal processes in the human body in different factual situations more simply than other existing models [3]. Due to the heterogeneous structure of the biological tissue and the occurrence of structural thermal interaction at various time scales, the Fourier's law of thermal conduction is improper for thermal analysis, and non-Fourier models should be used to obtain the heat distribution.

Among the various numerical methods for simulation of the hyperbolic equation system, the tendency is much more toward using methods that in addition to being simple and accurate, have a short runtime, and do not create unwanted numerical oscillations in the range of high discontinuities. The space–time CESE method proposed by Chang [4] to solve one-dimensional conservation equations has all the above features at the same time. By the mentioned method, the quantities of space and time behave precisely the same and differ in methodology and content from other numerical methods. This method emphasizes the integral form of the conservation equations, giving a more accurate simulation for the problems with significant discontinuities. In the CESE method, the unknown variables are first estimated using the first-order Taylor expansion in the solution elements (SEs). Then the conservation law is applied to each of the conservation elements (CEs). Poshti et al. [5] used two numerical methods, control volume (CV) and CESE method, to investigate the non-Fourier temperature distribution in 1-D spherical tissue based on the dual phase lag (DPL) model. Analyzing the results, the CESE method illustrates the highly discontinued areas without numerical oscillations as opposed to the CV method. In addition, the CESE method, due to its explicitness, requires less computational time than the CV method for the same number of mesh points.

Based on the space–time flux conservation and type of the governing equations, various schemes, such as $a - \mu$, a, and $a - \varepsilon$ that differ in obtaining unknown derivatives have been proposed in this method. The $a - \mu$ scheme is a basic scheme of the CESE method used to solve the 1-D convection–diffusion equation. In the a scheme of CESE method, which is the time-reversible, the flux conservation equations are written separately for the three existing CEs, and unknown variables are obtained from the combination of equations. In the case of the $a - \varepsilon$ scheme; obtaining a single conservation law around the combination of these CEs reduces the complexity of the solution. In this scheme, adjustable damping is added to the a scheme, so it can be used to solve irreversible problems.

Behaving similarly to 1-D and multidimensional problems, one of the characteristics of the CESE method, there is no need to apply dimensional splitting for solving multi-dimensional problems. The development of the space–time CESE method using tetrahedral meshes for solving 2-D Euler problems was proposed by Chang et al. [6, 7], and the results were investigated for a 2-D shock reflection problem. The primary building blocks for spatial meshes are triangular in the 2-D CESE method. Zhang et al. [8] developed this method with quadrilateral meshes, which creates, unlike the original method, four conservation elements in each mesh point and uses four mesh points at the previous time level to find unknown variables at present. Because of the simplicity, accuracy, and robustness of the $a - \varepsilon$ scheme, they have developed a 2-D case based on this scheme. Due to the simplicity and comprehensiveness of the CESE method in solving hyperbolic equations, many studies have been performed using structured and unstructured meshing in 2-D and 3-D Cartesian coordinates [9–13]. Weng and Gore [14] used the developed CESE method for simulating the 2-D and 3-D flow fields, that include detonation wave, shock wave, and expansion wave, in the pulse detonation engine. Chou and Yang [15] applied the developed CESE method to investigate non-Fourier behavior caused by laser irradiation in 2-D single and double-layer structures. Unlike other methods such as finite difference or control volume, by this method, the heat flux equations along the x and y directions with the energy equation are solved simultaneously at each time step.

Wang et al. [16, 17] presented an improved CESE method with a new structure of SEs and CEs. They used rectangular mesh to discretize the 2-D space domain and therefore the directions of space meshes, contrary to the original method, were perpendicular to each other and parallel to the main Cartesian axes. Simplifying the solution procedure, this method can be easily extended to 3-D scenarios. An improved CESE method has obtained favorable results in simulating various 2-D phenomena such as two-phase detonations [18], elastic–plastic flows [19], crystallization process [20], dam-break flows [21], shallow water problems [22], etc. Jiang et al. [23] utilized improved CESE method to solve 2-D and 3-D magnetohydrodynamic problems in general curvilinear coordinates by using the PARAMESH package for implementation of the parallel adaptive mesh refinement algorithm. Combining two half-time steps to perform integration on a full-time step, they eliminated the staggering nature of the space–time mesh structure in the original CESE method.

Comparing the results of numerical modeling with the data obtained from experiments plays a crucial role in designing an effective technique for thermal ablation of tumors. As an artificial structure, having the same characteristics as body tissue, such as optical, thermal, electrical, and acoustic properties, phantoms bring several advantages to experimental studies, including confirming the reliability of medical technologies, reducing the cost of experiments, and maintaining compatibility with living tissues. The literature contains many studies on the thermal and electrical behavior of tissue phantoms. For example, Paul et al. [24] experimentally and numerically studied the 3-D temperature distribution caused by laser irradiation in equivalent tissue phantoms with the presence and absence of blood vessels in the Cartesian coordinate system. Sahoo et al. [25] presented the theoretical and experimental results of temperature distribution in the cylindrical tissue phantom embedded with and without gold nanostructures and investigated the effects of thermal lagging in the tissue during laser irradiation. Singh et al. [26] designed a wireless multi-frequency electrical impedance tomography system in order to test and evaluate its performance on the phantoms with different inhomogeneities before applying it to the human body. In order to investigate different models of thermal conduction in the biological tissues, Li et al. [27] measured the temperature response due to focused ultrasound irradiation on cylindrical tissue phantom and ex vivo bovine liver tissue and compared the results with the predicted results by Fourier, thermal wave and DPL models.

A review of the applications of the CESE method in 2-D and 3-D Cartesian coordinates with quadrilateral and hexahedral meshes in previous studies confirms the ability of this method to supply acceptable results for solving hyperbolic problems. However, this method, despite many advantages over other numerical methods, has not yet been used in the multidimensional spherical coordinate system, therefore, in the present study, an attempt has been made to investigate the algorithm of the CESE method in 2-D spherical coordinates using polar meshes. Then, to confirm the proposed algorithm, the results obtained from modeling of non-Fourier thermal wave propagation due to laser irradiation on the spherical tissue surface are compared with both of semi-analytical results and experimental data measured by ultra-fast thermocouple during laser irradiation on the phantom surface. The proposed method provides the transient temperature and heat flux distribution in the spherical tissue along with an analysis of the non-Fourier thermal wave. Consequently, despite the 2-D effects of the thermal wave, makes it possible to predict the position of the maximum temperature in the tissue at different times.

2 Mathematical Model

At large scales, both temporally and spatially, the interaction between energy carriers is macroscopically expressed through Fourier's law. As stated by the theory of classical heat conduction (Fourier's law), the heat flux is proportional to the temperature gradient, and in 2-D spherical coordinates, this law describes:

$$\boldsymbol{q}(\boldsymbol{r}, t) = -k\nabla T(\boldsymbol{r}, t), \tag{1}$$

where t, k, and $\boldsymbol{r}$ are the time, thermal conductivity, and 2-D position vector (r, θ), respectively.

Nevertheless, in cases such as extremely short duration [28], very high-temperature gradient [29], temperatures near absolute zero [30], heat transfer in non-Newtonian fluids [31, 32], and thermal response of biological structures [33], the conventional theory of local equilibrium, or in other words the Fourier's law, is not applicable because the microstructural effects are dominated in the transient heat conduction. Tzou [34] proposed the DPL model to consider microstructural interactions of non-Fourier heat transfer, in which two phase lags τ_q and τ_T are introduced for heat flux and temperature gradient, respectively. Considering two phase lag times, the equation of the DPL model is mathematically expressed as follows:

$$\boldsymbol{q}\left(\boldsymbol{r}, t + \tau_q\right) = -k\nabla T(\boldsymbol{r}, t + \tau_{\mathrm{T}}). \tag{2}$$

According to Eq. (2), three characteristic times are defined, time t represents the transient heat transfer, time $t + \tau_T$ indicates the time at which the temperature gradient occurs in the material, and time $t + \tau_q$ denotes the time at which the heat flux flows [34]. By using first-order Taylor series, Eq. (2) can be expanded at radial (r) and angular (θ) directions in the spherical coordinates:

$$\boldsymbol{q}_{\mathbf{r}} + \tau_q \frac{\partial \boldsymbol{q}_{\mathbf{r}}}{\partial t} = -k\left[\frac{\partial T}{\partial r} + \tau_{\mathrm{T}} \frac{\partial^2 T}{\partial t \partial r}\right], \tag{3}$$

$$\boldsymbol{q}_{\boldsymbol{\theta}} + \tau_q \frac{\partial \boldsymbol{q}_{\boldsymbol{\theta}}}{\partial t} = -\frac{k}{r}\left[\frac{\partial T}{\partial \theta} + \tau_{\mathrm{T}} \frac{\partial^2 T}{\partial t \partial \theta}\right], \tag{4}$$

where $\boldsymbol{q}_{\boldsymbol{r}}$ and $\boldsymbol{q}_{\boldsymbol{\theta}}$ are the heat fluxes in the r and θ directions, respectively. Equations (3) and (4) become the classical Fourier equation with zero considering the phase lag times τ_T and τ_q.

Pennes equation has been applied to model the bio-heat transfer, as shown below [35]:

$$\rho c \frac{\partial T(\boldsymbol{r}, t)}{\partial t} = -\nabla \cdot \boldsymbol{q} + \omega_{\mathrm{b}} \rho_{\mathrm{b}} c_{\mathrm{b}} (T_{\mathrm{b}} - T) + Q_{\mathrm{m}} + Q_{\mathrm{ext}}, \tag{5}$$

where ρ is the density, c is the specific heat, ω_b denotes the perfusion rate of blood, Q_m denotes the metabolic heat generation, and Q_{ext} is the heat generated by external heat sources. The subscript b is related to the blood. This model considers the arterial system of tissue only composed of a capillary network. Due to this, the convective heat transfer between tissue and blood is negligible. In addition, conductive heat transfer in the blood and phase change in the tissue are neglected in this model. Therefore, the only mode of heat transfer between blood and tissue is blood perfusion to tissue, which is included in the Pennes equation.

Substituting the divergence in 2-D spherical coordinates to the right side of Eq. (5) gives:

$$\rho c \frac{\partial T(r, \theta, t)}{\partial t} = -\frac{2}{r}\boldsymbol{q}_{\boldsymbol{r}} - \frac{\partial \boldsymbol{q}_{\boldsymbol{r}}}{\partial r} - \frac{1}{r}\frac{\partial \boldsymbol{q}_{\boldsymbol{\theta}}}{\partial \theta} - \frac{Cot\theta}{r}\boldsymbol{q}_{\boldsymbol{\theta}} + \omega_b \rho_b c_b (T_b - T) + Q_m + Q_{\mathrm{ext}}. \tag{6}$$

Given that the laser irradiation is symmetrical concerning the φ direction and there will be variations only in the r and θ directions (see Fig. 1), the independent variables in the 3-D Euclidean space will be r, θ, and t. Since the behavior of time quantity is the same as spatial quantities in the CESE method, the 3-D element obtained to apply the flux conservation is similar to a cylindrical element having two longitudinal directions with one angular direction. For this reason, in order to use the divergence theorem, the governing equations must be written as cylindrical divergence. As a result, Eqs. (3), (4), and (6) can be rewritten in the following matrix form:

$$\frac{\partial \boldsymbol{U}}{\partial t} + \frac{1}{r}\frac{\partial}{\partial r}(r\boldsymbol{F}) + \frac{1}{r}\frac{\partial \boldsymbol{G}}{\partial \theta} = \boldsymbol{S}, \tag{7}$$

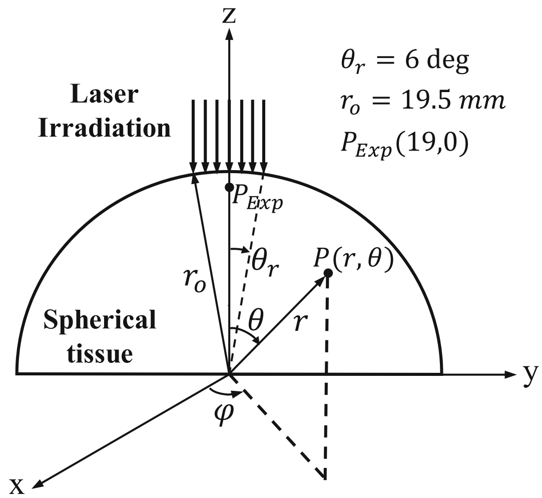

Fig. 1 Schematic geometry of symmetrical spherical tissue irradiated by laser light

where $\boldsymbol{U}$, $\boldsymbol{F}$, $\boldsymbol{G}$, and $\boldsymbol{S}$ are vectors of the primary variable, flux in r-direction, flux in θ-direction, and source, respectively:

$$\boldsymbol{U} = \begin{bmatrix} \frac{\boldsymbol{q}_{\boldsymbol{r}}}{r} \\ \boldsymbol{q}_{\boldsymbol{\theta}} \\ T \end{bmatrix}, \tag{8}$$

$$\boldsymbol{F} = \begin{bmatrix} \frac{k}{\tau_q r}\left(T + \tau_T \frac{\partial T}{\partial t}\right) \\ 0 \\ \frac{\boldsymbol{q}_{\boldsymbol{r}}}{\rho c} \end{bmatrix}, \tag{9}$$

$$\boldsymbol{G} = \begin{bmatrix} 0 \\ \frac{k}{\tau_q}\left(T + \tau_T \frac{\partial T}{\partial t}\right) \\ \frac{\boldsymbol{q}_{\boldsymbol{\theta}}}{\rho c} \end{bmatrix}, \tag{10}$$

$$\boldsymbol{S} = \begin{bmatrix} -\frac{\boldsymbol{q}_{\boldsymbol{r}}}{\tau_q r} \\ -\frac{\boldsymbol{q}_{\boldsymbol{\theta}}}{\tau_q} \\ \frac{1}{\rho c}\left(\omega_b \rho_b c_b (T_b - T) + Q_m - \frac{\boldsymbol{q}_{\boldsymbol{r}}}{r} - \frac{Cot\theta}{r}\boldsymbol{q}_{\boldsymbol{\theta}}\right) \end{bmatrix}. \tag{11}$$

Given that the physical variables and their first-order derivatives are unknowns in the CESE method, all unknown quantities must be determined at time $t = 0$. In this study, the initial temperature of tissue phantom is equal to 24.3°C, and other initial conditions can be gained by:

$$\frac{\partial T}{\partial r}, \frac{\partial T}{\partial \theta}, \boldsymbol{q}_{\boldsymbol{r}}, \frac{\partial \boldsymbol{q}_{\boldsymbol{r}}}{\partial r}, \frac{\partial \boldsymbol{q}_{\boldsymbol{r}}}{\partial \theta}, \boldsymbol{q}_{\boldsymbol{\theta}}, \frac{\partial \boldsymbol{q}_{\boldsymbol{\theta}}}{\partial r}, \frac{\partial \boldsymbol{q}_{\boldsymbol{\theta}}}{\partial \theta}(r, \theta, 0) = 0. \tag{12}$$

Because the wavelength of the laser irradiated on the tissue is in the infrared region, the highly absorbed situation occurs, and the majority of the laser heat flux is absorbed within the minimal thickness at the tissue surface [36]. Thus

Q_{ext} is omitted from Eq. (6), and the laser effect is assumed to be the constant heat flux boundary condition at the tissue surface ($r = r_o$). Equation (3) calculates the temperature gradient in the radial direction by determining the radial heat flux at the surface of the tissue as well as initial conditions. Then the temperature at the tissue surface is obtained using a backward differential scheme. In order to determine the temperature gradient in angular direction at the tissue surface, the backward differential scheme for time can be used in Eq. (4). Other unknown quantities at $r = r_o$ can be determined as:

$$\frac{\partial \boldsymbol{q_r}}{\partial r}, \frac{\partial \boldsymbol{q_r}}{\partial \theta}, \boldsymbol{q_\theta}, \frac{\partial \boldsymbol{q_\theta}}{\partial r}, \frac{\partial \boldsymbol{q_\theta}}{\partial \theta}(r_o, \theta, t) = 0. \tag{13}$$

As seen in Fig. 1, the symmetry boundary condition is established at $\theta = 0$. Therefore, the values of $\boldsymbol{q_r}$, $\partial \boldsymbol{q_r}/\partial r$, T and $\partial T/\partial r$ at point $(r, 0)$ are equal to the corresponding values at point $(r, \Delta\theta)$ and other unknown quantities can be determined as:

$$\frac{\partial \boldsymbol{q_r}}{\partial \theta}, \boldsymbol{q_\theta}, \frac{\partial \boldsymbol{q_\theta}}{\partial r}, \frac{\partial \boldsymbol{q_\theta}}{\partial \theta}, \frac{\partial T}{\partial \theta}(r, 0, t) = 0. \tag{14}$$

In the center of the spherical tissue, the insulation boundary condition can be adopted, in which case the temperature at the center of the tissue is equal to the temperature at the radius $r = \Delta r$, and other unknown quantities can be given as:

$$\boldsymbol{q_r}, \frac{\partial \boldsymbol{q_r}}{\partial r}, \frac{\partial \boldsymbol{q_r}}{\partial \theta}, \boldsymbol{q_\theta}, \frac{\partial \boldsymbol{q_\theta}}{\partial r}, \frac{\partial \boldsymbol{q_\theta}}{\partial \theta}, \frac{\partial T}{\partial r}, \frac{\partial T}{\partial \theta}(0, \theta, t) = 0. \tag{15}$$

Assuming no heat loss from the surface of the tissue and also being the angular heat flux at $\theta = 0$ equal to zero due to symmetry; therefore, the output thermal boundary condition is considered at $\theta = \pi/2$. In this case, the values of $\boldsymbol{q_r}$, $\partial \boldsymbol{q_r}/\partial r$, $\boldsymbol{q_\theta}$, $\partial \boldsymbol{q_\theta}/\partial r$, T and $\partial T/\partial r$ at point $(r, \pi/2)$ are equal to the corresponding values at point $(r, \pi/2 - \Delta\theta)$ and other unknown quantities can be determined as:

$$\frac{\partial \boldsymbol{q_r}}{\partial \theta}, \frac{\partial \boldsymbol{q_\theta}}{\partial \theta}, \frac{\partial T}{\partial \theta}(r, \pi/2, t) = 0. \tag{16}$$

3 CESE Scheme with Polar Space Mesh

The processing steps of the CESE method begin with transforming the differential form of the governing equations into integral form equations. The next step is to divide the space—time domain using conservation and solution elements and approximate the unknown variables by the first-order Taylor expansion in the solution elements, followed by determining relationships between spatial and temporal derivatives. The final step includes obtaining the unknown variables by transforming the volume integral into the surface integral around the conservation elements using divergence law.

The original CESE method uses three-dimensional octagonal meshes in which the two space directions are neither perpendicular to each other nor along the coordinate axes, resulting in complexity in the solution process. However, the improved CESE method uses hexagonal meshes, which can easily be extended to three-dimensional because of its two perpendicular space directions. In this study, polar meshes have been used to solve equations in the 2-D spherical coordinate system, which formed a cylindrical segment in three-dimensional Euclidean space E_3 (whose coordinates are defined as $x_1 = r$, $x_2 = \theta$, $x_3 = t$). Therefore, it is unnecessary to convert the equations from the spherical coordinate system to the Cartesian system or to use unstructured meshes. By using the Gaussian divergence theorem in the Euclidean space E_3, Eq. (7) can be transformed into integral conservation form as below [4]:

$$\oint_{S(V)} \boldsymbol{H}_m \cdot \mathrm{d}\boldsymbol{s} = \int_V S_m \mathrm{d}V, \tag{17}$$

where $m = 1, 2, 3$ represents the number of primary variables, and $\boldsymbol{H}_m = (F_m, G_m, U_m)$ is the space–time flux vector, where F_m, G_m, and U_m are the components of the vector $\boldsymbol{F}$, $\boldsymbol{G}$, and $\boldsymbol{U}$, respectively. $S(V)$ is the boundary of arbitrary space–time domain V in the Euclidean space E_3, $d\boldsymbol{s} = d\sigma.\boldsymbol{n}$ is the surface element on $S(V)$ in which $d\sigma$ is the area and $\boldsymbol{n}$ is the outward unit normal of the surface element, and S_m are the components of the source vector $\boldsymbol{S}$.

The spatial domain is divided into staggered mesh points at different time levels. In the two-dimensional scheme of the CESE method, (i, j, n) represents a set of space–time mesh points in E_3, where $n = 0, \pm 1/2, \pm 1, \ldots$ for time, $i = n \pm 1/2, n \pm 3/2, \ldots$ for r and $j = n \pm 1/2, n \pm 3/2, \ldots$ for θ. The projection of the mesh points on the $r-\theta$ plane is shown in Fig. 2a, where the interval between the hollow circle points and the solid circle points in the time direction is equal to $\Delta t/2$. The solution element corresponding to mesh point (i, j, n) is represented as $SE(i, j, n)$, and as shown in Fig. 2b, it consists of a curved plane $BB''F''F$ and two flat planes, $A'C'E'G'$ and $HH''D''D$, having intersection point $P'(i, j, n)$. Similarly, there are four solution elements corresponding to the other points A, C, E, and G, which are at the time level $n - 1/2$. The total space–time domain is divided into non-overlapping conservation elements. The corresponding conservation element of point P' is denoted by $CE(i, j, n)$, which is formed as a cylindrical segment, $ACEGA'C'E'G'$, with the surfaces associated with $SE(P')$ and the surfaces associated with the four solution elements at the previous time level, $SE(A)$, $SE(C)$, $SE(E)$ and $SE(G)$ (see Fig. 2c). Since the surfaces of the CEs are along the

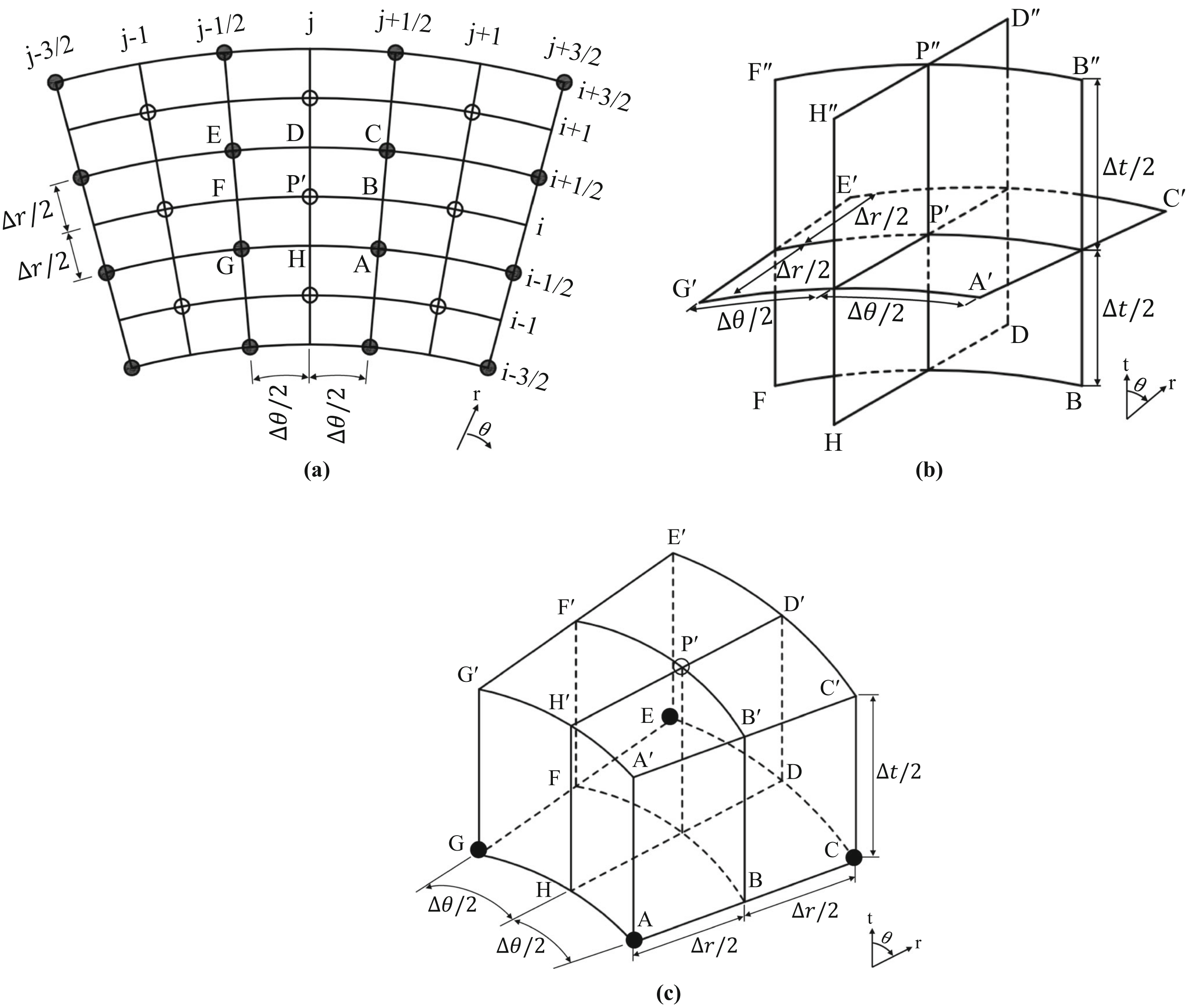

Fig. 2 Schematic illustration of the space–time domain and primary elements in the developed CESE method with polar space mesh, **a** 2-D staggered mesh points, **b** solution element, and **c** conservation element

unit vectors in the r, θ, and t directions, the normal vectors of each surface of the CEs are along one of the coordinate axes. Thus, only a single component of the total flux h is considered in the calculation of the output space–time flux from each surface.

Due to define the $SE\left(P'\right)$ for an arbitrary mesh point $P'(i,\ j,\ n)$, the variables U_m, F_m, and G_m using a first-order Taylor expansion can be approximated as follows [17]:

$$U_m\left(\delta r,\ \delta\theta,\ \delta t\right)_{P'} \equiv \left[U_m\left(\delta r,\ \delta\theta,\ \delta t\right)\right]^n_{i,\,j} = \left(U_m\right)_{P'} + \left(U_{mr}\right)_{P'}\delta r + \left(U_{m\theta}\right)_{P'}\delta\theta + \left(U_{mt}\right)_{P'}\delta t. \tag{18}$$

The expressions for F_m and G_m can also be written similarly. Here $\delta r = r - r_{P'}$, $\delta\theta = \theta - \theta_{P'}$ and $\delta t = t - t_{P'}$; $r_{P'}$, $\theta_{P'}$ and $t_{P'}$ are the position coordinates at the P' mesh point. Subscript P' represents the value of the variables mentioned and their derivatives with respect to r, θ, and t at mesh point P'. Since F_m and G_m are a function of U_m, their derivatives can be obtained using the chain rule:

$$F_{mr} = \sum_{l=1}^{3}\frac{\partial F_m}{\partial U_l}\frac{\partial U_l}{\partial r},\ F_{m\theta} = \sum_{l=1}^{3}\frac{\partial F_m}{\partial U_l}\frac{\partial U_l}{\partial\theta},\ F_{mt} = \sum_{l=1}^{3}\frac{\partial F_m}{\partial U_l}\frac{\partial U_l}{\partial t}. \tag{19}$$

The derivatives of G_m can be obtained in an analogous way. In phenomena similar to thermal waves, the governing equations are stiff in nature, meaning that the source term time scale is very small compared to the time scale of convective heat transfer [37]. As a result, in numerical calculations, the source term only affects mesh points that are at the new time level, and no effect of the source term is present in determining the values of U_{mt} at the previous time level. Therefore, as stated by Eq. (7), the values of U_{mt} at points A, C, E, and G are determined:

$$U_{mt} = -\frac{1}{r}F_m - F_{mr} - \frac{1}{r}G_{m\theta}. \tag{20}$$

Note that Eqs. (18)–(20) show that the only unknown variables in the CESE method are U_m, U_{mr}, and $U_{m\theta}$. According to the definition of CE at the mesh point P', Eq. (17) can be rewritten as:

$$\oint_{S(CE(P'))} \boldsymbol{H}_m \cdot \mathrm{d}\boldsymbol{s} = (S_m)_{P'} r_{P'} \Delta r \Delta\theta \frac{\Delta t}{2}. \tag{21}$$

Integrating Eq. (21) on the surfaces of $CE(P')$ with the assistance of Eq. (18) yields the following expression:

$$\begin{aligned} r_i (U_m)^n_{i,j} &+ \frac{\Delta r^2}{12}(U_{mr})^n_{i,j} - \frac{\Delta t}{2} r_i (S_m)^n_{i,j} \\ &= \sum_{p=\mp 1;\, q=\mp 1} \Bigg\{ -q\frac{\Delta t}{4\Delta\theta}\left[G_m\left(-p\frac{\Delta r}{4}, 0, \frac{\Delta t}{4}\right)\right]^{n-1/2}_{ip,\,jq} \\ &\quad - p\frac{\Delta t}{4\Delta r} r_{ip}\left[F_m\left(0, -q\frac{\Delta\theta}{4}, \frac{\Delta t}{4}\right)\right]^{n-1/2}_{ip,\,jq} \\ &\quad + \frac{1}{4} r_{ip}\left[U_m\left(-p\frac{\Delta r}{4}, -q\frac{\Delta\theta}{4}, 0\right)\right]^{n-1/2}_{ip,\,jq} + \frac{\Delta r^2}{48}(U_{mr})^{n-1/2}_{ip,\,jq} \Bigg\} \\ &\quad + \frac{\Delta\theta\Delta r}{64}\left[\sum_{p=1;\, q=\mp 1} q(U_{m\theta})^{n-1/2}_{ip,\,jq} - \sum_{p=-1;\, q=\mp 1} q(U_{m\theta})^{n-1/2}_{ip,\,jq}\right], \end{aligned} \tag{22}$$

where $ip = i + p/2$and $jq = j + q/2$are considered to shorten the equation. Given the values of U_m, U_{mr}, and $U_{m\theta}$ at the time level $n - 1/2$, the right side of Eq. (22) are known; on the other hand, according to Eq. (11), the source vector of $\boldsymbol{S}$on the left side is a linear function of U_m, so only two quantities $U_m$and $U_{mr}$are unknown that must be obtained.

The central difference scheme can be used to calculate U_{mr} and $U_{m\theta}$ if there is no discontinuity in the solution range:

$$(U_{mr})^n_{i,j} = \frac{\left(U'_m\right)^n_{i+1/2,\,j} - \left(U'_m\right)^n_{i-1/2,\,j}}{\Delta r}, \tag{23}$$

$$(U_{m\theta})^n_{i,j} = \frac{\left(U'_m\right)^n_{i,\,j+1/2} - \left(U'_m\right)^n_{i,\,j-1/2}}{\Delta\theta}, \tag{24}$$

where U'_m is determined by first-order Taylor expansion over time:

$$\left(U'_m\right)^n_{i\pm 1/2,\,j} = (U_m)^{n-1/2}_{i\pm 1/2,\,j} + \frac{\Delta t}{2}(U_{mt})^{n-1/2}_{i\pm 1/2,\,j}, \tag{25}$$

$$\left(U'_m\right)^n_{i,\,j\pm 1/2} = (U_m)^{n-1/2}_{i,\,j\pm 1/2} + \frac{\Delta t}{2}(U_{mt})^{n-1/2}_{i,\,j\pm 1/2}. \tag{26}$$

In the event of discontinuity, the use of the central difference scheme causes unrealistic wiggles in the solution, so the weighted difference scheme must be used to obtain the unknown derivatives [4]:

$$(U_{mr})^n_{i,j} = W\left[(U_{mr-})^n_{i,j}, (U_{mr+})^n_{i,j}, \alpha\right], \tag{27}$$

$$(U_{m\theta})^n_{i,j} = W\left[(U_{m\theta-})^n_{i,j}, (U_{m\theta+})^n_{i,j}, \alpha\right], \tag{28}$$

where α is an adjustable parameter such that $\alpha \geq 0$ and the quantities $(U_{mr\pm})^n_{i,j}$ and $(U_{m\theta\pm})^n_{i,j}$ as well as the weight function W are defined as follows:

$$(U_{mr\pm})^n_{i,j} = \pm\left[\left(U'_m\right)^n_{i\pm 1/2,\,j} - (U_m)^n_{i,j}\right]/(\Delta r/2), \tag{29}$$

$$(U_{m\theta\pm})^n_{i,j} = \pm\left[\left(U'_m\right)^n_{i,\,j\pm 1/2} - (U_m)^n_{i,j}\right]/(\Delta\theta/2), \tag{30}$$

$$W\left[x_-, x_+, \alpha\right] = \frac{|x_+|^\alpha x_- + |x_-|^\alpha x_+}{|x_+|^\alpha + |x_-|^\alpha}. \tag{31}$$

The procedure of solving is such that first an initial value for $(U_{mr})^n_{i,j}$ is assumed, then the value of $(U_m)^n_{i,j}$ is obtained using Eq. (22), and finally, employing Eqs. (23)–(31), new values of $(U_{mr})^n_{i,j}$ as well as $(U_{m\theta})^n_{i,j}$ will be determined. This process continues until the values obtained for $(U_{mr})^n_{i,j}$ converge. In the present study, the linear approximation with the finite difference scheme is used to determine the initial

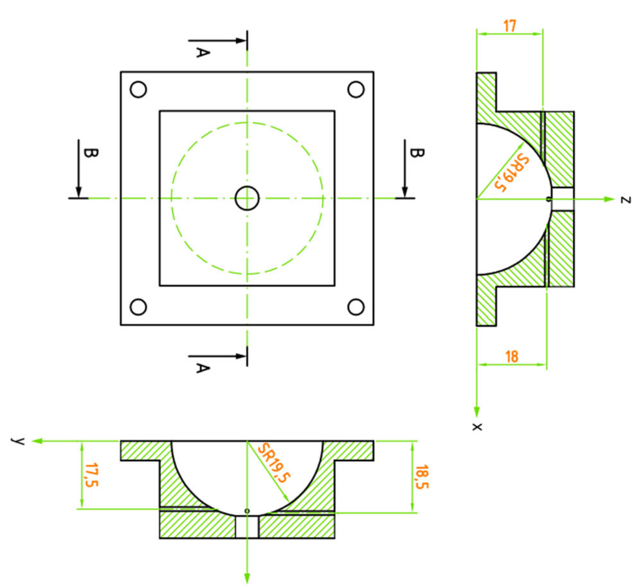

Fig. 3 Upper hemisphere map with embedded holes for thermocouple placement

values of $(U_{mr})^n_{i,j}$ to avoid iterative procedures in solving and to reduce computational time.

$$(U_{mr})^n_{i,j} = \frac{1}{2\Delta r}\left\{\sum_{p=1;q=\mp1}\left[U_m\left(0,\,0,\,\frac{\Delta t}{2}\right)\right]^{n-1/2}_{ip,\,jq} - \sum_{p=-1;q=\mp1}\left[U_m\left(0,\,0,\,\frac{\Delta t}{2}\right)\right]^{n-1/2}_{ip,\,jq}\right\}, \quad (32)$$

where $ip = i+p/2$and $jq = j+q/2$are considered to shorten the equation. On the other hand, due to the discontinuity at an angular direction on the surface of the tissue, the weighted difference scheme is used to obtain the derivatives, and the value of α is considered to be 1. In the numerical results, the values obtained with linear approximation are consistent with the results of the iterative procedure, which indicates that the approximation used is perfectly rational.

Since $r = 0$ is a singular point of the $\boldsymbol{U}$ and $\boldsymbol{S}$ matrices, two mesh points with $r = \Delta r/20$ which is very close to the points with $r = 0$, and two mesh points with $r = \Delta r$ are used to determine the unknown variables in the calculations at the mesh point with $r = \Delta r/2$.

4 Experimental Method

Due to the fact that different effective parameters are out of control in natural tissues, phantoms equivalent to biological tissues are used to investigate the thermal behaviors. In order to confirm the numerical results obtained through the CESE method, experiments on the phantoms with optical tissue characteristics have been performed in the Optical Bio-Imaging (OBI) laboratory of the Laser and Plasma Research Institute at Shahid Beheshti University.

Gel phantoms are made from a combination of 80% distilled water, 20% Intralipid in volume, and 5wt.% agarose [38]. Making an Intralipid phantom includes these steps: distilled water is boiled first, then Intralipid is added and boiled with distilled water for a short time. The agar powder is then mixed with the prepared solution, and the existing mixture is stirred continuously to obtain a homogeneous solution. The resulting solution is poured into a mold and is kept in the refrigerator. Subsequently, the hardened phantom can be used after 24 hours. Adding agar powder to an Intralipid phantom causes it to solidify while not having a significant effect on its absorption coefficient.

In order to create a tissue phantom in a spherical shape, the standard ping-pong ball with an inner diameter of 39mm is used as the mold. Two hemispherical parts, 39mm in diameter, are designed to perform laser irradiation experiments on spherical tissue phantom. These two Teflon parts are fastened together by bolts and nuts after placing the phantom inside them. The use of Teflon material not only prevents the chemical reaction of the phantom with it, but also insulates the test conditions. The sensor (MLT1402 T-type Ultra-Fast Thermocouple Probe, response time 0.005s, accuracy ±0.1°C, ADInstruments) and laser are respectively connected to the phantom from the side and top walls of the upper hemispherical part. On the side walls of the upper part, four holes with a diameter of 1mm are considered; which are used to insert the T-type thermocouple with a supplied 23ga. hypodermic needle (Terumo Corporation, Laguna, Philippines) into the tissue phantom at position $\theta = 0°$. The center of these holes is located at distances of 17.5, 18, 18.5, and 19mm along the z-axis from the base surface of the upper hemispherical part, as shown in Fig. 3. The thermocouple data are recorded and saved using a National Instruments Data Acquisition system (NI SCB-68A) and LabVIEW software. The schematic of the experimental setup and spherical Intralipid phantom are shown in Fig. 4.

The pulsed laser used in this study has a wavelength of 1550nm, a pulse duration of 18ms, and an average intensity of 2100Wm^{-2}. The laser is irradiated to the spherical tissue surface using fiber with a diameter of 20 microns at the position $\theta = 0°$, so one M6 thread is placed on the upper hemisphere to stabilize the tip of the fiber. Based on data presented in Refs. [39, 40], around the wavelength of 1550 nm, the impact of the absorption coefficient of biological tissues is significantly greater than the scattering coefficient. In this case, it can be assumed that a thin layer on the tissue surface absorbs all the laser energy, and the effect of radiation can be applied as a constant heat flux on the tissue surface. As a result, if the diffuse reflectance of the laser light at the irradiated surface and the intensity of the laser are denoted by R and q_L, respectively, the constant heat flux boundary condition $q_a = q_L(1-R)$ is considered at the tissue surface.

5 Result and Discussion

The CESE method is developed to solve non-Fourier heat conduction equations caused by laser irradiation on biological tissue in the 2-D spherical coordinate system using polar mesh points. Since there is no similar numerical study on 2-D spherical coordinates to verify the performance of the developed CESE method using polar mesh points, the obtained dimensionless temperatures (θ) are compared with the semi-analytical results presented by Ramadan [41] in 1-D spherical coordinates, as shown in Fig. 5. Dimensionless quantities of radius and time are denoted by ζ and η, respectively. A pulsed heat flux with a pulse duration of $\eta_s = 0.2$ is applied to the outer surface of the tissue. It is clear that the results obtained from the CESE method with polar mesh points are almost consistent with the existing 1-D semi-analytical results. To have a more detailed review, a number of these results are

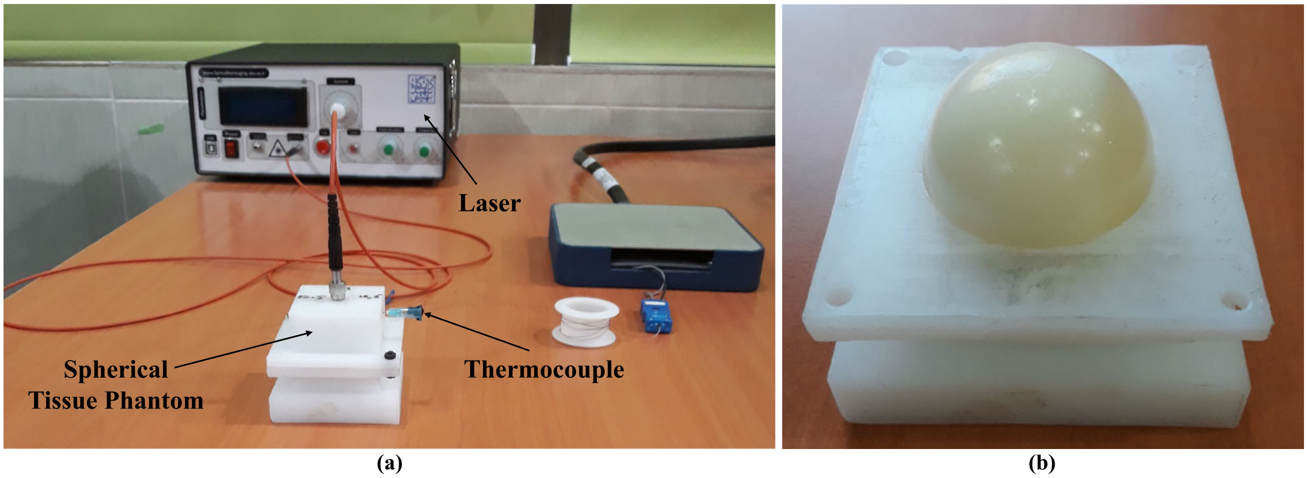

Fig. 4 **a** Experimental setup for tissue phantom irradiation using 1550 nm laser, **b** Spherical Intralipid phantom

compared at two times $\eta = 0.8$ and $\eta = 0.9$ in Tables 1 and 2, respectively.

Also, an in vitro experiment is performed on spherical Intralipid phantoms exposed to laser irradiation. The laser is irradiated on the tissue phantom surface with an initial temperature of $T_i = 24.3°\mathrm{C}$ and a radius of $r_o = 1.95\mathrm{cm}$ for $t_r = 180\mathrm{s}$. The diffuse reflectance of the laser light at the tissue phantom surface is $R = 0.05$ [36], and the effects of the laser irradiation are investigated until the final time $t_f = 420\mathrm{s}$. The thermo-physical properties used in the present study are listed in Table 3. According to the studies [33, 42–44], both phase lag times of temperature gradient and heat flux for the tissues are in the range of 0.01 to 32s. In the current study, phase lag times are considered to be $\tau_T = 2\mathrm{s}$ and $\tau_q = 16\mathrm{s}$ [45]. Given that the effects of blood perfusion and metabolic heat generation are not present in the tissue phantoms, these two terms are omitted from Eq. (6) in numerical calculations.

In the following, numerical results are examined for spherical tissue phantom with the radius of $r_o = 1.95\mathrm{cm}$, which is exposed to laser irradiation at the sector of $0 < \theta < 6°$ on its surface (Fig. 1). The significant discontinuity along θ direction is well simulated using the CESE method without generating numerical wiggles in the solution. The following dimensionless parameters are used in the presented results for generality:

$$\Phi = \frac{T - T_i}{T_{\max} - T_i},\ \eta = \frac{t}{t_f},\ \zeta = \frac{r}{r_o},\quad Q_r = \frac{\boldsymbol{q_r}}{q_a},\quad Q_\theta = \frac{\boldsymbol{q}_\theta}{q_a},\ \theta^* = \frac{\theta}{\theta_t} \tag{33}$$

where T_{max} is the maximum temperature generated in the tissue phantom during laser irradiation, and θ_t is the reference angle equal to 90°.

The mesh independency of the numerical results in the two directions, r and θ, is shown in Fig. 6. To investigate the effect of the grid size in the radial direction, the temperature graph is given by the radius for the different mesh resolutions, at angle $\theta^* = 0$ and at time $\eta = 0.3$ (Fig. 6a). As can be seen, by increasing the mesh resolution in the radial direction, the results are entirely consistent with each other, so the number of radial mesh points in the calculations is considered as 400 nodes. In addition, to evaluate the effect of the number of mesh points used in θ direction on the results, the surface temperature ($\zeta = 1$) variation at time $\eta = 0.3$ is displayed in Fig. 6b for the different mesh resolutions in the angular direction. It is apparent that by increasing the number of mesh points, the results are not significantly different; thus 100 nodes in the θ direction are used for the

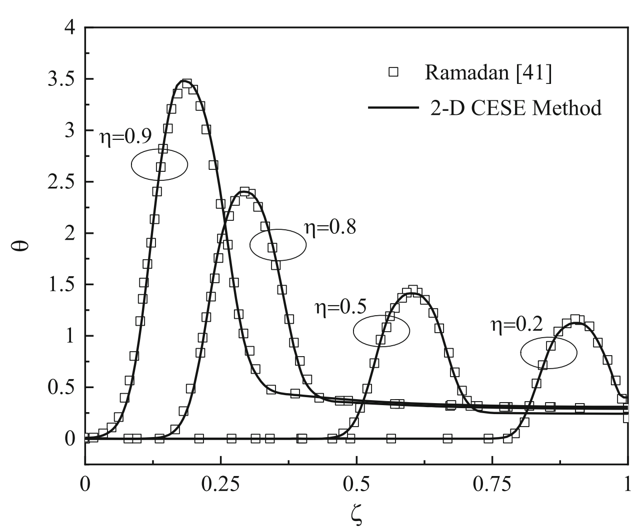

Fig. 5 Temperature distributions of pulsed heat flux at different dimensionless times

Table 1 Comparison between CESE method and semi-analytical results at time $\eta = 0.8$

ζ	0.13	0.21	0.29	0.37	0.45
2-D CESE method	0.0062	0.7274	2.4013	1.2565	0.3842
Semi-analytical [41]	0	0.7642	2.3816	1.3112	0.3868

Table 2 Comparison between CESE method and semi-analytical results at time $\eta = 0.9$

ζ	0.02	0.1	0.18	0.26	0.34
2-D CESE method	0.0172	0.9871	3.4672	1.9467	0.4683
Semi-analytical [41]	0.0185	1.0344	3.4048	1.9158	0.4982

Table 3 Thermo-physical properties of tissue and blood [36, 44, 46]

Parameters	Tissue	Blood
Density/ kgm^{-3}	1000	1060
Specific heat/ $Jkg^{-1}K^{-1}$	4187	3860
Thermal conductivity/ $Wm^{-1}K^{-1}$	0.628	–
Metabolic heat generation/ Wm^{-3}	1190	–
Blood perfusion rate/ s^{-1}	0.00187	–
Blood temperature/ °C	–	37

numerical simulations. It should be noted that the time step is $\Delta\eta = 2.6 \times 10^{-5}$.

The experimental transient temperature measured by an ultra-fast thermocouple at the point $P_{Exp}(19, 0)$ inside the spherical tissue phantom (see Fig. 1) is plotted with the 2-D numerical results obtained by the developed CESE method in Fig. 7. The experiment was repeated three times and average results were reported. Savitzky-Golay smoothing filter with polynomial order of 2 and 400 points of window is applied to reduce the effects of noise on experimental thermocouple data. Comparing experimental and numerical transient temperature distribution demonstrates that the results agree well with each other. It should be noted that applying the thermo-physical properties used in the literature for the tissue phantom, assuming the value of two time lag constants related to the temperature gradient and the heat flux, and existing unavoidable measurement errors in experiments are effective in creating differences between the experimental data and the calculated results. In addition, while a part of the laser energy is lost in actual conditions, it is assumed that the laser heat flux is completely absorbed on the surface of the tissue phantom in the calculations. Also, other mechanisms of the heat transfer caused by laser irradiation, such as natural convection, evaporative cooling, and water evaporation, are not taken into account. Finally, the subsurface location of the thermocouple in performing the experiment test on the spherical Intralipid phantom, which is a mechanically soft material, may not be accurate, and hence slight discrepancies between experimental measurements and numerical results can be seen.

2-D heat flux and temperature contours at time $\eta = 0.4$ during irradiation and times $\eta = 0.45$ and 0.5 after stopping irradiation are shown in Figs. 8–10. The angle of irradiation ($\theta_r = 6°$) is specified in these figures for better display. It should be noted that the irradiation time is $\eta_r = 0.43$. As shown in Fig. 8a, at time $\eta = 0.4$ during laser irradiation, the maximum value of Q_r is on the surface of the tissue phantom, and its value decreases toward the center of the tissue. When irradiation is interrupted, the maximum value of Q_r is not at the surface, and the radial heat flux wave propagates in the tissue phantom (see Fig. 8b and c). Comparison of Fig. 8a, b, and c shows that the intensity of the radial heat flux wave decreases with its propagation inside the tissue. In order to better display the radial heat flux wave propagation, the Q_r distribution in the radial direction at angles $\theta^* = 0$ and 0.07 for different times η is presented in Fig. 8d. Evidently, the heat flux Q_r decreases with rising θ^* at times $\eta = 0.4$ and 0.45, but the 2-D effects of the thermal wave at time $\eta = 0.5$ cause the Q_r values to increase at angle $\theta^* = 0$ to 0.07.

The evolution of the 2-D angular heat flux field in spherical tissue phantom at time $\eta = 0.4$ during laser irradiation and times $\eta = 0.45$ and 0.5 after laser interruption is illustrated in Fig. 9. Due to the fact that laser irradiation is uniform in the angular segment $0 < \theta < 6°$, the maximum value of angular heat flux is not around the laser irradiation area, unlike the radial heat flux distribution in Fig. 8a. The presence of irradiation discontinuity on the surface at the angle of $\theta = 6°$ causes the temperature gradient variation, i.e., $\partial\Phi/\partial\theta$, to be high, hence the maximum value of Q_θ occurs in this region, as shown in Fig. 9a. It can be seen in Fig. 9b and c that the angular heat flux wave propagates in r and θ directions at times after stopping the laser irradiation, and the intensity

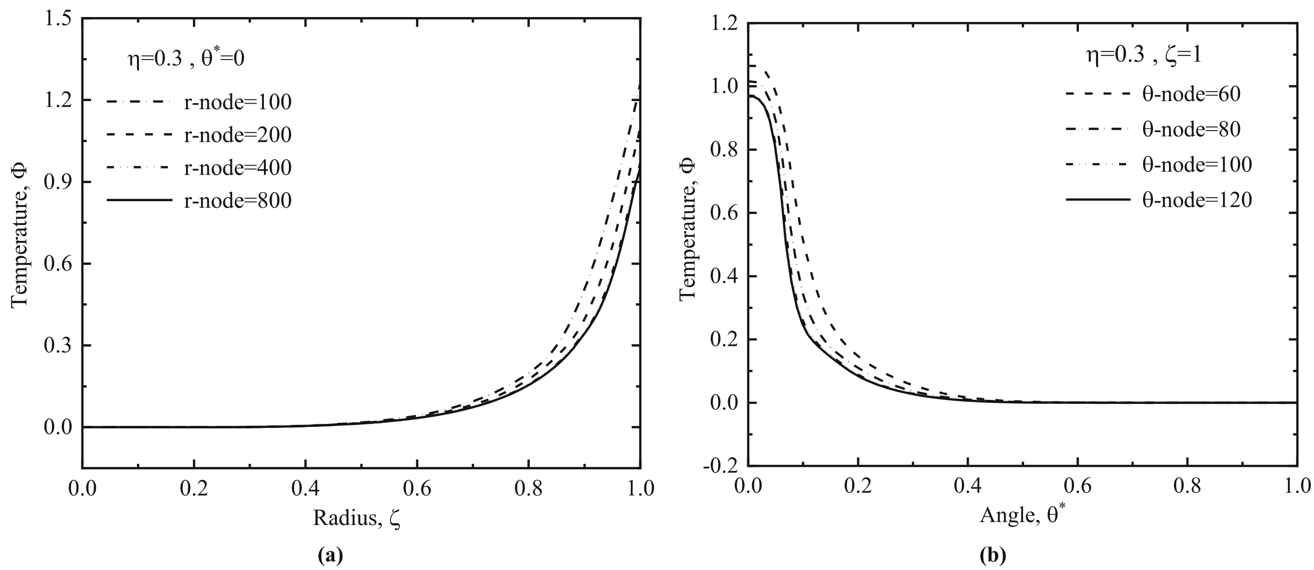

Fig. 6 Comparison of the effects of the mesh points number in the, **a** radial direction and **b** angular direction on the numerical results

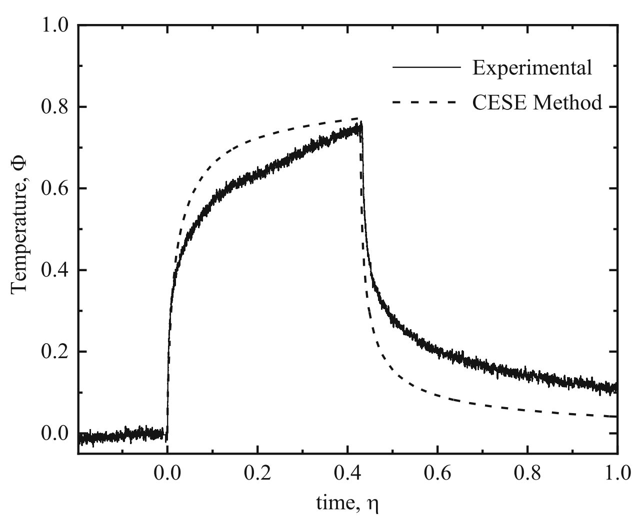

Fig. 7 Comparison of transient temperature distribution at the point $P_{Exp}(19, 0)$ inside the spherical tissue phantom

of the heat flux wave reduces due to the effects of diffusion in the tissue.

Comparison of Figs. 8 and 9 show that the ratio of the values of angular to radial heat flux (Q_θ/Q_r) has increased in the tissue over time so that these values are close to each other at time $\eta = 0.5$. Therefore, the effects of angular and radial heat flux at this time are such that the angular heat flux prevails in the region behind the wave front. As seen in Fig. 8c, in this region, the direction of radial heat flux vector has changed toward the surface of the tissue. To better display the angular heat flux wave propagation in the tissue, the Q_θ distribution in the angular direction for radii $\zeta = 1$ and 0.95 at different times η is indicated in Fig. 9d. It is observed that the angular heat flux Q_θ decreases with increasing ζ at times $\eta = 0.4$, 0.45, and 0.5.

In hyperthermia treatment planning, accurate prediction and control of temperature distribution are essential to rise the temperature locally in the tumoral tissue without damaging adjacent healthy tissues. Non-dimensional temperature distributions corresponding to different times $\eta = 0.4$, 0.45, and 0.5 are shown in Fig. 10. It can be seen in Fig. 10a, at time $\eta = 0.4$, the surface temperature increases from the initial temperature to more than 90% of the maximum temperature during the irradiation process. It should be point out that the temperature increase in the tissue reaches its peak at time $\eta_r = 0.43$, when the laser irradiation continues on its surface. As shown in Fig. 10b and c, at times $\eta = 0.45$ and 0.5 after stopping the irradiation, heat penetrates toward the center of the tissue phantom due to the diffusion behavior and affects most areas of the tissue. According to Fig. 10b and c, it can be seen that the interference of two heat flux waves that propagate along the r and θ directions, has disturbed the temperature distribution. As a result, the propagation of the thermal wave in both radial and angular directions will cause the formation of the low-temperature region behind the wave front and the diffusion of the thermal wave front to the tissue surface (see Fig. 10c).

Temperature distribution at various times for radii $\zeta = 1$ and $\zeta = 0.95$ in Fig. 10d demonstrates that the maximum temperature at the tissue surface ($\zeta = 1$) during laser irradiation is at angle $\theta^* = 0$. However, by interrupting the laser irradiation, the 2-D effects of the thermal wave cause the

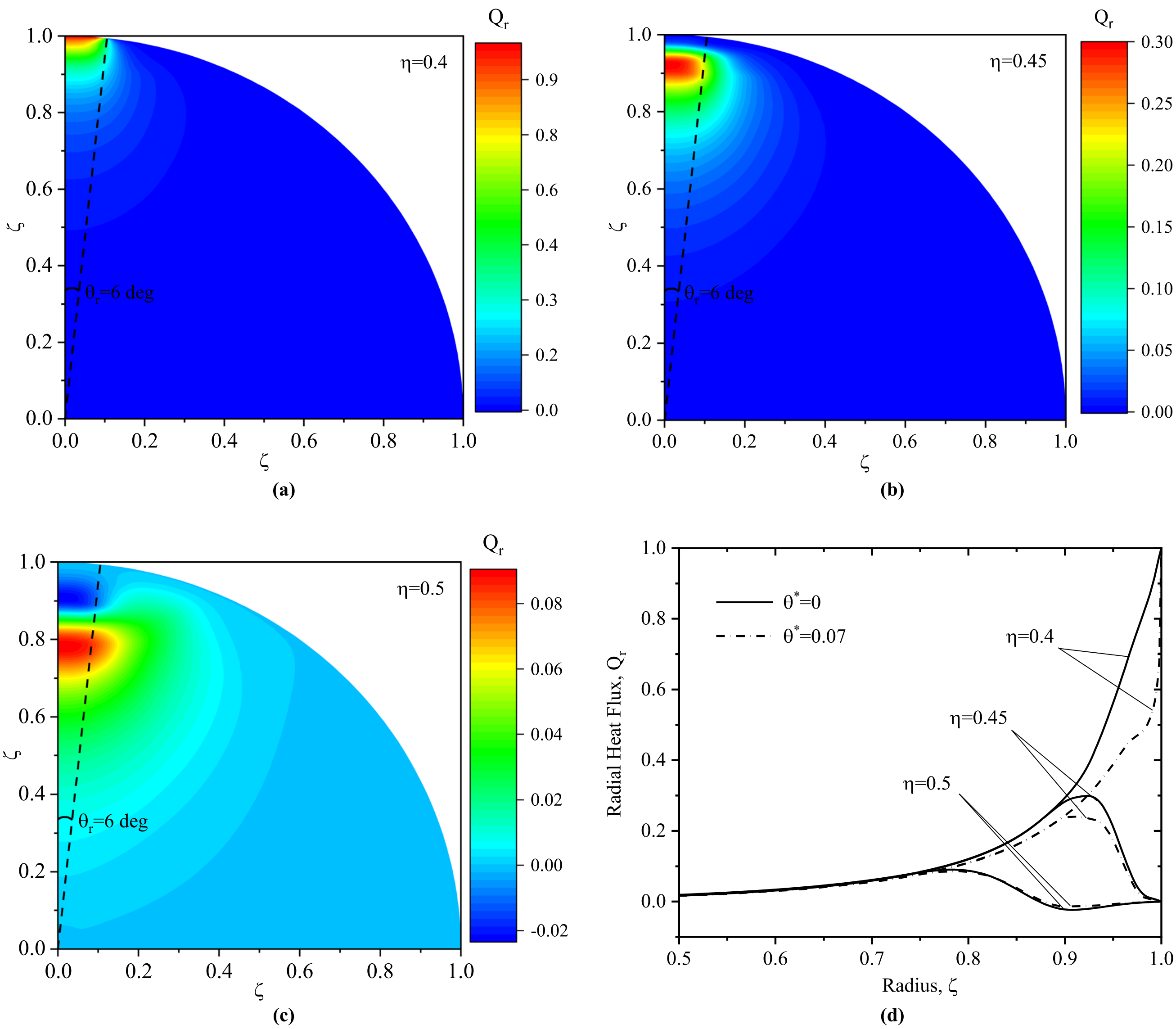

Fig. 8 Contours of radial heat flux Q_r at different times, **a** $\eta = 0.4$, **b** $\eta = 0.45$, and **c** $\eta = 0.5$. **d** Comparison of radial heat flux distribution at various times for angles $\theta^* = 0$ and $\theta^* = 0.07$

maximum surface temperature to move and occur at $\theta^* > 0$. The results show that the temperature at the radius $\zeta = 1$ is higher than the radius $\zeta = 0.95$ during irradiation ($\eta = 0.4$). However, the propagation of the thermal wave in the tissue at time $\eta = 0.45$ causes the temperature distribution at the radius $\zeta = 1$ to be less than $\zeta = 0.95$. Then, by creating 2-D effects of thermal wave in the tissue at time $\eta = 0.5$, the temperature profiles approach each other.

Figure 11 shows the progress of the thermal wave and position of maximum temperature in tissues including muscle, tumor, and fat at the angle $\theta^* = 0$ at different times $\eta = 0.42$, 0.44, 0.46, and 0.48 considering the same temperature range for all tissues and similar maximum temperature in numerical calculations. Table 4 illustrates the thermo-physical properties applied for different tissues in this simulation.

Thermal diffusivity of the tissue is a single effective parameter in speed of the thermal wave propagation as all three tissues have the same values of temperature gradient and heat flux phase lags. In addition, two parameters of metabolic heat generation and blood perfusion are neutral in determination of the maximum temperature location in the tissue. Among sample tissues, the maximum and minimum thermal diffusivity belongs to tumor and fat tissue, respectively. Thus, as shown in Fig. 11, the wave progression in fat tissue is less than in other tissues at the same time, while the most significant wave movement is in the tumor tissue.

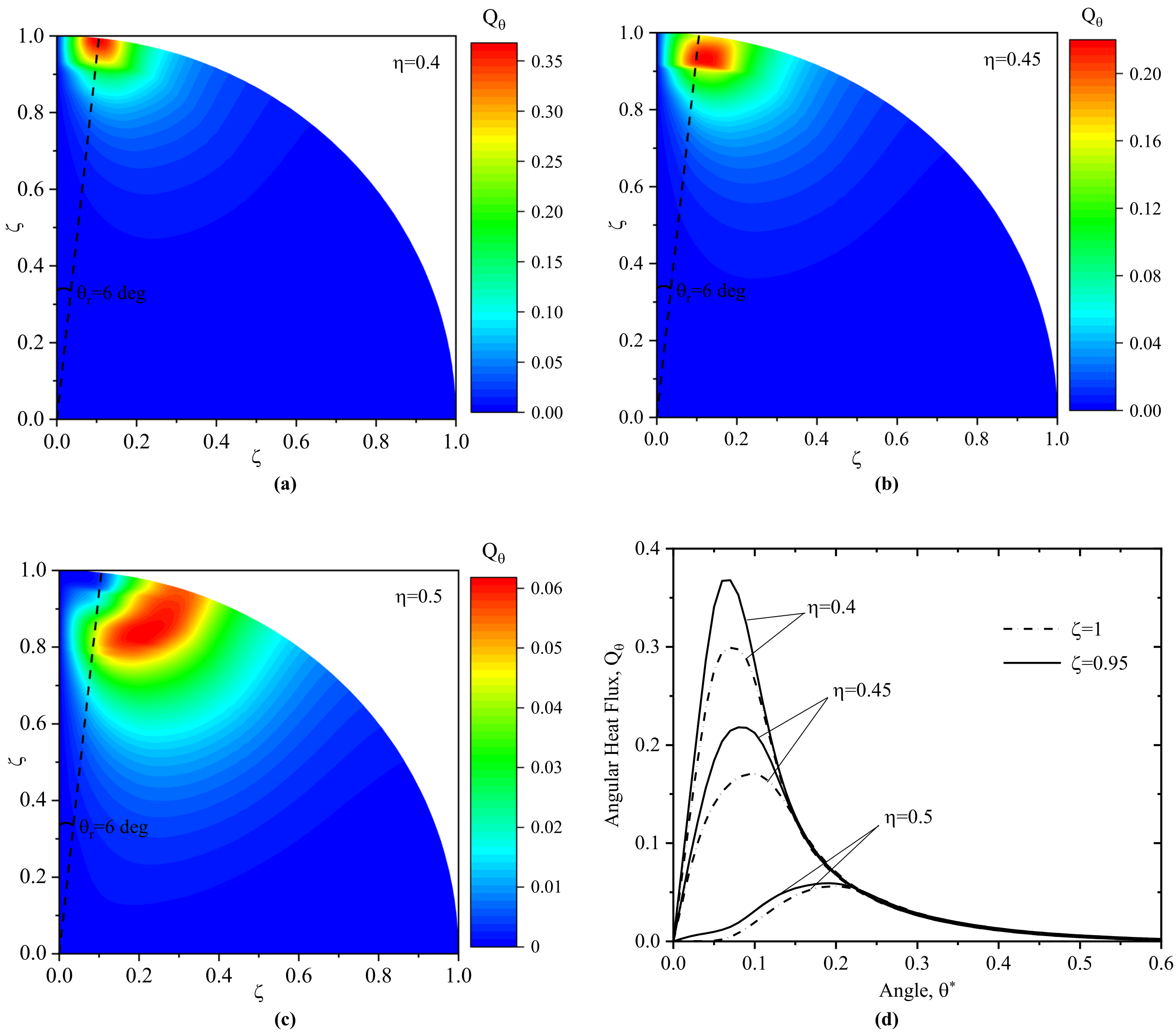

Fig. 9 Contours of angular heat flux Q_θ at different times, **a** $\eta = 0.4$, **b** $\eta = 0.45$, and **c** $\eta = 0.5$. **d** Comparison of angular heat flux distribution at various times for radii $\zeta = 1$ and $\zeta = 0.95$

Furthermore, due to thermal diffusivity, tendency of tissue in transferring the energy to absorb, fat tissue with lowest thermal diffusivity is expected to reach the highest temperature values. Comparing the temperature distributions of various tissues in Fig. 11 confirms the mentioned results.

6 Conclusion

In this article, an improved 2-D space–time CESE method in Cartesian coordinates using quadrilateral meshes is developed to solve hyperbolic equation system in the 2-D spherical coordinate system using polar meshes. The developed CESE method has been used to investigate non-Fourier thermal wave propagation in spherical tissue due to laser irradiation on its surface. Applying the proposed uncomplicated and highly accurate approach, there is no need to use the general coordinate system and transfer the equations to the Cartesian coordinate system. A comparison of temperature distribution obtained using the developed CESE method with the available semi-analytical results shows that this method is capable of analyzing non-Fourier thermal wave problems based on the DPL model. The experimental test is then performed to investigate the transient temperature distribution caused by laser irradiation in the spherical Intralipid phantom. A comparison of the numerical findings with the data obtained from

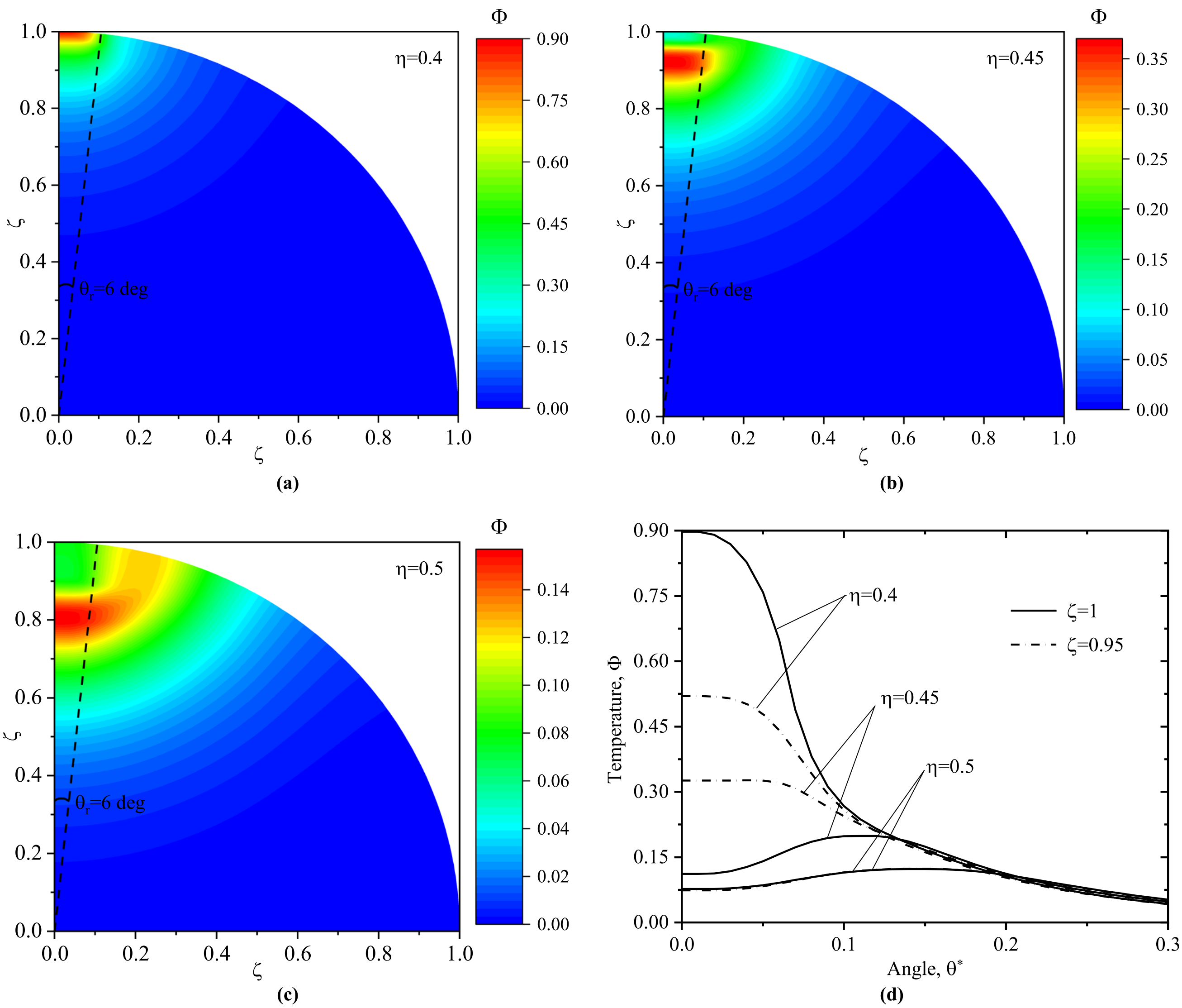

Fig. 10 Contours of non-dimensional temperature Φ at different times, **a** $\eta = 0.4$, **b** $\eta = 0.45$, and **c** $\eta = 0.5$. **d** Comparison of temperature distribution at various times for radii $\zeta = 1$ and $\zeta = 0.95$

the experiments confirms the use of the non-Fourier DPL model in the simulation of heat transfer in biological tissues. Therefore, utilizing numerical simulations, the thermal behavior of tissues in hyperthermia treatment is predictable to achieve desire thermal distribution by changing the effective parameters in clinical studies. Following this research, the transient profiles of heat fluxes and temperature in the tissue phantom are investigated to determine the phenomenon of thermal wave propagation inside the tissue. The results signify that the propagation of the thermal wave in both radial and angular directions affects the temperature distribution in the tissue. The effects of angular heat flux increase over time, altering the direction of the radial heat flux, and the temperature drops in the region behind the wave front. Furthermore, the investigation of thermal wave propagation in different tissues indicates that the higher the thermal diffusivity, the greater the wave progression within the tissue, and the more regions are affected by laser irradiation. In contrast, temperature values in the tissue with the lowest thermal diffusivity are minimum among all.

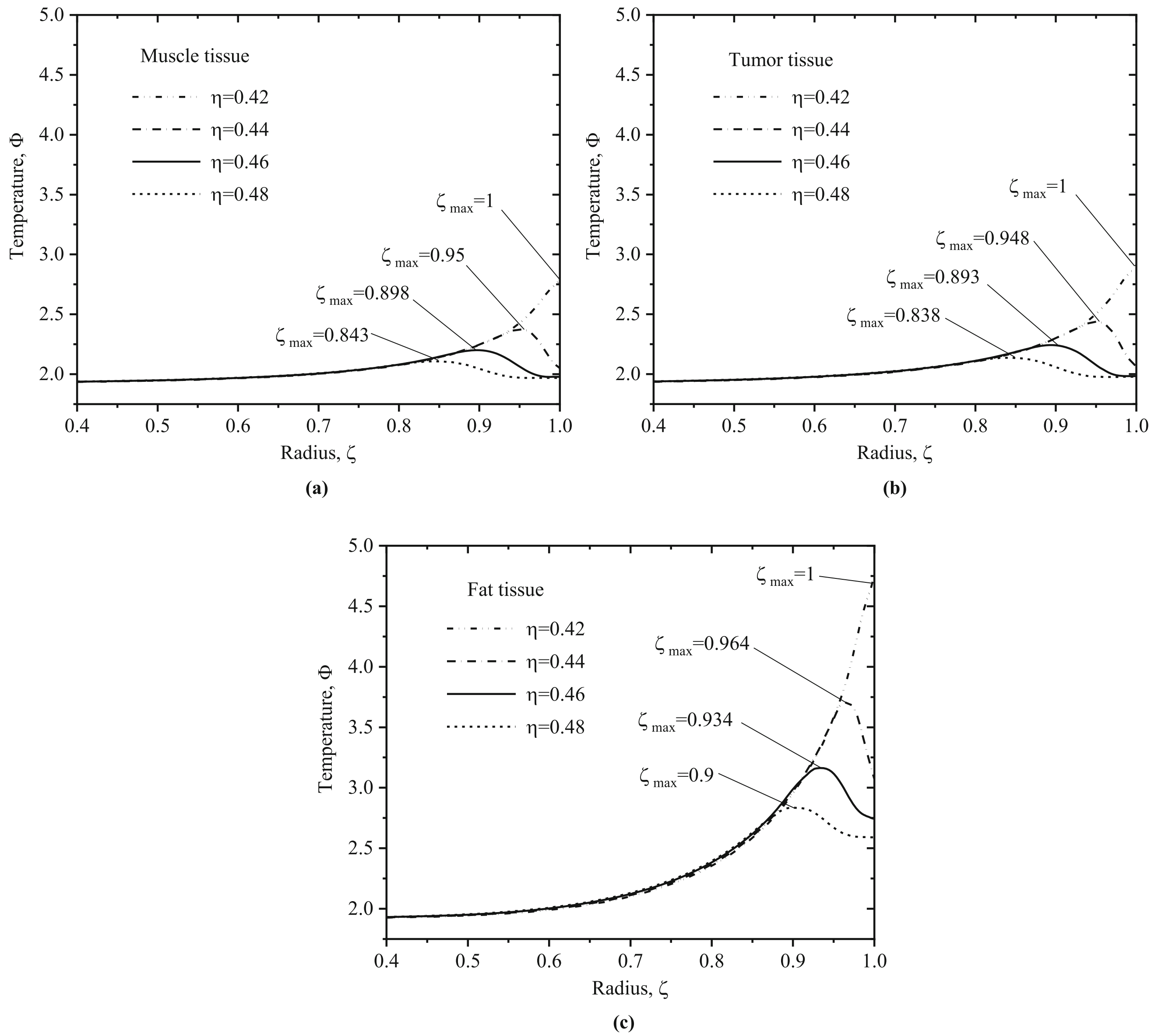

Fig. 11 Comparison of propagation of thermal wave along with $\theta^* = 0$ at different times in, **a** muscle, **b** tumor, and **c** fat tissue

Table 4 Thermo-physical properties of tissues

Tissue type	Thermal conductivity/$Wm^{-1}K^{-1}$	Density/kgm^{-3}	Specific heat/$Jkg^{-1}K^{-1}$	Blood perfusion rate/s^{-1}	Metabolic heat generation/Wm^{-3}	Refs.
Muscle	0.628	1000	4187	0.00187	1190	[44]
Tumor	0.5641	1020	3510	0.00066	480	[47]
Fat	0.185	971	2700	0	368.3	[48]

Acknowledgements Author M.A.A. was supported by Grant No. 98029460 of Iranian National Science Foundation (INSF).

Declarations

Conflict of interest The authors have no competing interests to declare that are relevant to the content of this article.

References

1. Dhar, P.; Paul, A.; Narasimhan, A.; Das, S.K.: Analytical prediction of sub–surface thermal history in translucent tissue phantoms during plasmonic photo–thermotherapy (PPTT). J. Therm. Biol. **62**, 143–149 (2016). https://doi.org/10.1016/j.jtherbio.2016.06.023
2. Kumar, D.; Rai, K.: A study on thermal damage during hyperthermia treatment based on DPL model for multilayer tissues using finite element Legendre wavelet Galerkin approach. J. Therm. Biol. **62**, 170–180 (2016). https://doi.org/10.1016/j.jtherbio.2016.06.020
3. Turkyilmazoglu, M.: Heat transfer from warm water to a moving foot in a footbath. Appl. Therm. Eng. **98**, 280–287 (2016). https://doi.org/10.1016/j.applthermaleng.2015.12.027
4. Chang, S.C.: The method of space-time conservation element and solution element—a new approach for solving the Navier-Stokes and Euler equations. J. Comput. Phys. **119**(2), 295–324 (1995). https://doi.org/10.1006/jcph.1995.1137
5. Poshti, A.G.T.; Khosravirad, A.; Ayani, M.B.: Analyses of non-Fourier heat conduction in 1-D spherical biological tissue based on dual-phase-lag bio-heat model using the conservation element/solution element (CE/SE) method: a numerical study. Int. Commun. Heat Mass Transf. **132**, 105881 (2022)
6. Chang, S.C.; Wang, X.Y.; Chow, C.Y.: The method of space-time conservation element and solution element-applications to one-dimensional and two-dimensional time-marching flow problems. In: 12th Computational Fluid Dynamics Conference, p. 1754 (1995). https://doi.org/10.2514/6.1995-1754
7. Chang, S.C.; Wang, X.Y.; Chow, C.Y.: The space-time conservation element and solution element method: a new high-resolution and genuinely multidimensional paradigm for solving conservation laws. J. Comput. Phys. **156**(1), 89–136 (1999). https://doi.org/10.1006/jcph.1999.6354
8. Zhang, Z.C.; Yu, S.J.; Chang, S.C.: A space-time conservation element and solution element method for solving the two-and three-dimensional unsteady Euler equations using quadrilateral and hexahedral meshes. J. Comput. Phys. **175**(1), 168–199 (2002). https://doi.org/10.1006/jcph.2001.6934
9. Zhang, Z.C.; Yu, S.; Wang, X.Y.; Chang, S.C.; Himansu, A.; Jorgenson, P.: The CE/SE method for Navier-Stokes equations using unstructured meshes for flows at all speeds. In: 38th Aerospace Sciences Meeting and Exhibit, p. 393 (2000). https://doi.org/10.2514/6.2000-393
10. Zhang, Z.C.; Yu, S.; He, H.; Chang, S.C.: Direct calculations of two-and three-dimensional detonations by an extended CE/SE method. In: 39th Aerospace Sciences Meeting and Exhibit, p. 476 (2001). https://doi.org/10.2514/6.2001-476
11. Qamar, S.; Mudasser, S.: On the application of a variant CE/SE method for solving two-dimensional ideal MHD equations. Appl. Numer. Math. **60**(6), 587–606 (2010). https://doi.org/10.1016/j.apnum.2010.02.005
12. Chang, C.L.; Choudhari, M.M.: Hypersonic viscous flow over large roughness elements. Theor. Comput. Fluid Dyn. **25**(1–4), 85–104 (2011). https://doi.org/10.1007/s00162-010-0191-9
13. Shen, H.; Wen, C.Y.; Saldívar Massimi, H.: Application of CE/SE method to study hypersonic non-equilibrium flows over spheres. In: 19th AIAA International Space Planes and Hypersonic Systems and Technologies Conference, p. 2509 (2014). https://doi.org/10.2514/6.2014-2509
14. Weng, C.; Gore, J.P.: A numerical study of two-and three-dimensional detonation dynamics of pulse detonation engine by the CE/SE method. Acta Mech. Sin. **21**(1), 32–39 (2005). https://doi.org/10.1007/s10409-004-0004-8
15. Chou, Y.; Yang, R.J.: Two-dimensional dual-phase-lag thermal behavior in single-/multi-layer structures using CESE method. Int. J. Heat Mass Transf. **52**(1), 239–249 (2009). https://doi.org/10.1016/j.ijheatmasstransfer.2008.06.025
16. Gang, W.; De-Liang, Z.; Kai-Xin, L.: An improved CE/SE scheme and its application to detonation propagation. Chin. Phys. Lett. **24**(12), 3563 (2007). https://doi.org/10.1088/0256-307X/24/12/074
17. Wang, G.; Zhu, H.; Sun, Q.; Zhang, D.; Liu, K.: An improved CE/SE scheme and its application to dilute gas–particle flows. Comput. Phys. Commun. **182**(8), 1589–1601 (2011). https://doi.org/10.1016/j.cpc.2011.04.004
18. Wang, G.; Zhang, D.; Liu, K.; Wang, J.: An improved CE/SE scheme for numerical simulation of gaseous and two-phase detonations. Comput. Fluids **39**(1), 168–177 (2010). https://doi.org/10.1016/j.compfluid.2009.07.010
19. Wang, J.; Liu, K.; Zhang, D.: An improved CE/SE scheme for multi-material elastic–plastic flows and its applications. Comput. Fluids **38**(3), 544–551 (2009). https://doi.org/10.1016/j.compfluid.2008.04.014
20. Noor, S.; Qamar, S.: Solution of a multi-dimensional batch crystallization model with fines dissolution using CE/SE method. Life Sci. J. **23**, 337–341 (2014)
21. Zhang, Y.; Zeng, Z.; Chen, J.: The improved space–time conservation element and solution element scheme for two-dimensional dam-break flow simulation. Int. J. Numer. Methods Fluids **68**(5), 605–624 (2012). https://doi.org/10.1002/fld.2525
22. Qamar, S.; Warnecke, G.: Application of space–time CE/SE method to shallow water magnetohydrodynamic equations. J. Comput. Appl. Math. **196**(1), 132–149 (2006). https://doi.org/10.1016/j.cam.2005.08.014
23. Jiang, C.; Feng, X.; Zhang, J.; Zhong, D.: AMR simulations of magnetohydrodynamic problems by the CESE method in curvilinear coordinates. Sol. Phys. **267**(2), 463–491 (2010). https://doi.org/10.1007/s11207-010-9649-6
24. Paul, A.; Narasimhan, A.; Kahlen, F.J.; Das, S.K.: Temperature evolution in tissues embedded with large blood vessels during photo-thermal heating. J. Therm. Biol. **41**, 77–87 (2014). https://doi.org/10.1016/j.jtherbio.2014.02.010
25. Sahoo, N.; Ghosh, S.; Narasimhan, A.; Das, S.K.: Investigation of non-Fourier effects in bio-tissues during laser assisted photothermal therapy. Int. J. Therm. Sci. **76**, 208–220 (2014). https://doi.org/10.1016/j.ijthermalsci.2013.08.014
26. Singh, G.; Anand, S.; Lall, B.; Srivastava, A.; Singh, V.: A low-cost portable wireless multi-frequency electrical impedance tomography system. Arab. J. Sci. Eng. **44**(3), 2305–2320 (2019). https://doi.org/10.1007/s13369-018-3435-4
27. Li, C.; Miao, J.; Yang, K.; Guo, X.; Tu, J.; Huang, P., et al.: Fourier and non-Fourier bio-heat transfer models to predict ex vivo temperature response to focused ultrasound heating. J. Appl. Phys. **123**(17), 174906 (2018)
28. Qiu, T.; Tien, C.: Heat transfer mechanisms during short-pulse laser heating of metals. J. Heat Transf. **115**(4), 835–841 (1993). https://doi.org/10.1115/1.2911377
29. Maurer, M.; Thompson, H.: Non-Fourier effects at high heat flux. J. Heat Transf. **95**(2), 284–286 (1973). https://doi.org/10.1115/1.3450051

30. Cimmelli, V.A.; Frischmuth, K.: Hyperbolic heat conduction at cryogenic temperatures. Reniconti Del Circolo Matematico Di Palermo. **45**, 137–145 (1996)
31. Turkyilmazoglu, M.: Heat transfer enhancement feature of the Non-Fourier Cattaneo-Christov heat flux model. J. Heat Transf. **143**(9), 094501 (2021)
32. Jafarimoghaddam, A.; Turkyilmazoglu, M.; Pop, I.: Threshold for the generalized Non-Fourier heat flux model: Universal closed form analytic solution. Int. Commun. Heat Mass Transf. **123**, 105204 (2021)
33. Antaki, P.J.: New interpretation of non-Fourier heat conduction in processed meat. J. Heat Transf. **127**(2), 189–193 (2005). https://doi.org/10.1115/1.1844540
34. Tzou, D.Y.: Macro-to Microscale Heat Transfer: The Lagging Behavior. Wiley, Chichester (2015)
35. Pennes, H.H.: Analysis of tissue and arterial blood temperatures in the resting human forearm. J. Appl. Physiol. **1**(2), 93–122 (1948). https://doi.org/10.1152/jappl.1948.1.2.93
36. Liu, K.C.: Analysis for high-order effects in thermal lagging to thermal responses in biological tissue. Int. J. Heat Mass Transf. **81**, 347–354 (2015). https://doi.org/10.1016/j.ijheatmasstransfer.2014.10.035
37. Yu, S.T.; Chang, S.C.; Yu, S.T.; Chang, S.C.: Treatments of stiff source terms in conservation laws by the method of space-time conservation element/solution element. In: 35th Aerospace Sciences Meeting and Exhibit, p. 435 (1997). https://doi.org/10.2514/6.1997-435
38. Masoumi, S.; Ansari, M.A.; Mohajerani, E.; Genina, E.A.; Tuchin, V.V.: Combination of analytical and experimental optical clearing of rodent specimen for detecting beta-carotene: phantom study. J. Biomed. Opt. **23**(9), 095002 (2018)
39. Vuylsteke, M.; Van Dorpe, J.; Roelens, J.; De Bo, T.; Mordon, S.: Endovenous laser treatment: a morphological study in an animal model. Phlebology **24**(4), 166–175 (2009). https://doi.org/10.1258/phleb.2009.008070
40. Alemzadeh-Ansari, M.J.; Ansari, M.A.; Zakeri, M.; Haghjoo, M.: Influence of radiant exposure and repetition rate in infrared neural stimulation with near-infrared lasers. Lasers Med. Sci. **34**(8), 1555–1566 (2019). https://doi.org/10.1007/s10103-019-02741-4
41. Ramadan, K.: Semi-analytical solutions for the dual phase lag heat conduction in multilayered media. Int. J. Therm. Sci. **48**(1), 14–25 (2009). https://doi.org/10.1016/j.ijthermalsci.2008.03.004
42. Zhou, J.; Chen, J.; Zhang, Y.: Dual-phase lag effects on thermal damage to biological tissues caused by laser irradiation. Comput. Biol. Med. **39**(3), 286–293 (2009). https://doi.org/10.1016/j.compbiomed.2009.01.002
43. Zhang, Y.: Generalized dual-phase lag bioheat equations based on nonequilibrium heat transfer in living biological tissues. Int. J. Heat Mass Transf. **52**(21–22), 4829–4834 (2009). https://doi.org/10.1016/j.ijheatmasstransfer.2009.06.007
44. Kaminski, W.: Hyperbolic heat conduction equation for materials with a nonhomogeneous inner structure. J. Heat Transf. **112**(3), 555–560 (1990). https://doi.org/10.1115/1.2910422
45. Zhou, J.; Zhang, Y.; Chen, J.: An axisymmetric dual-phase-lag bioheat model for laser heating of living tissues. Int. J. Therm. Sci. **48**(8), 1477–1485 (2009). https://doi.org/10.1016/j.ijthermalsci.2008.12.012
46. Mitra, K.; Kumar, S.; Vedevarz, A.; Moallemi, M.: Experimental evidence of hyperbolic heat conduction in processed meat. J. Heat Transf. **117**(3), 568–573 (1995). https://doi.org/10.1115/1.2822615
47. Converse, M.; Bond, E.J.; Hagness, S.C.; Van Veen, B.D.: Ultrawide-band microwave space-time beamforming for hyperthermia treatment of breast cancer: a computational feasibility study. IEEE Trans. Microw. Theory Tech. **52**(8), 1876–2189 (2004). https://doi.org/10.1109/TMTT.2004.832012
48. Xu, F.; Seffen, K.; Lu, T.: Non-Fourier analysis of skin biothermomechanics. Int. J. Heat Mass Transf. **51**(9–10), 2237–2259 (2008). https://doi.org/10.1016/j.ijheatmasstransfer.2007.10.024